



The genesis and environmental context of hypogene-sourced terrestrial carbonates of the middle Pleistocene in Vedi, Ararat Depression

Shlomy Vainer ^a, Alex Brittingham ^b, Theodoros Karampaglidis ^{c,*}, Boris Gasparyan ^d, Artur Petrosyan ^d, Hayk Haydosyan ^d, Dmitri Arakelyan ^e, Yael Kiro ^f, Yonatan Goldsmith ^g, Ariel Malinsky-Buller ^b

^a Department of Earth and Environmental Sciences, Ben-Gurion University of the Negev, Beer-Sheva, Israel

^b The Institute of Archaeology, The Hebrew University of Jerusalem, Jerusalem, Israel

^c Department of Geological and Mining Engineering, University of Castilla-La Mancha, Toledo, Spain

^d Institute of Archaeology and Ethnography, National Academy of Sciences of the Republic of Armenia, Yerevan, Armenia

^e Institute of Geological Sciences, National Academy of Sciences of the Republic of Armenia, Yerevan, Armenia

^f Department of Earth and Planetary Sciences, Weizmann Institute of Science, Rehovot, Israel

^g Institute of Earth Sciences, The Hebrew University of Jerusalem, Jerusalem, Israel

ARTICLE INFO

Handling Editor: Dr Donatella Magri

ABSTRACT

The Ararat Depression (Armenia), situated between the southern Caucasus and northern Mesopotamia, holds substantial archaeological Middle Paleolithic sites. However, as paleoclimate archives are scarce in the region, the climatic history is not well constrained. To reconstruct the local paleoclimatic conditions in the past, we studied a ~30 m-thick sequence of carbonates deposited in the Vedi Valley, a tributary of the Ararat Valley. We applied field mapping, petrography, geochemistry, stable isotope analysis, and U-Th dating to investigate the genesis and evolution of these carbonates. Two main facies are identified: (1) a micritic-peloidal microbial facies formed in low-energy palustrine settings, and (2) a sparitic calcite facies formed via CO₂ degassing from deeply sourced hypogene fluids. δ¹³C and δ¹⁸O values, together with elemental proxies, indicate early closed-system degassing of hydrothermal solutions interacting with marine carbonates of the Yerakh Anticline, followed by increased meteoric influence and detrital input in the upper portion of the sequence.

Three distinct detrital units coincide with heavier δ¹⁸O and lighter δ¹³C values and likely reflect wetter intervals during interglacial phases. Isochron U-Th dating constrains deposition to occur between 319 ± 84 and 198 ± 14 ka, corresponding to Marine Isotope Stages (MIS) 9–7. The results indicate that the Vedi Valley carbonates constitute a Middle Pleistocene sequence formed under the combined influence of active tectonics, volcanism, and climatic shifts. As such, they provide a rare archive of landscape evolution in a region critical for understanding past environmental variability and human dispersal pathways.

1. Introduction

Terrestrial carbonates precipitated from spring-fed systems are valuable archives of past environmental conditions, recording changes in groundwater sources, hydrochemistry, and surface connectivity (Andrews, 2006; Pentecost and Viles, 1994; Alonso-Zarza and Tanner, 2009). These deposits are especially informative in tectonically active and semi-arid regions, where lake or speleothem records are often discontinuous and reworked. In such settings, carbonates precipitated

from groundwater-fed systems can preserve proxies informing of hydrological shifts, tectonic activity, and climatic variability.

The Vedi Valley in the Ararat Depression (Armenia) contains a ~30 m-thick sequence of middle Pleistocene carbonates formed in a fault-controlled spring-marsh system. Located at the interface of major biogeographic zones in the southern Caucasus, the basin lies along an active tectonic corridor shaped by Quaternary volcanism, strike-slip faulting, and fluctuating hydrological regimes (Karakhanyan et al., 2016; Avagyan et al., 2018; Karampaglidis et al., 2025). The Vedi record

This article is part of a special issue entitled: Southern Caucasus published in Quaternary Science Reviews.

* Corresponding author.

E-mail address: theo.Karampaglidis@uclm.es (T. Karampaglidis).

offers an opportunity to reconstruct landscape evolution for understanding ecological thresholds, climate-tectonic interactions, and spring persistence under variable conditions. However, interpreting such records requires careful discrimination between input from biotic and abiotic precipitation processes, surface epigean waters or deep hypogean waters, and the degrees of mixing and diagenesis, all of which may vary over time (Freytet and Verrecchia, 2002; Pentecost, 2005; Alonso-Zarza, 2003).

To interpret the depositional archive, we distinguish between biotic and abiotic precipitation through carbonate fabric. Biotic structures typically reflect microbial mediation by Cyanobacteria, Chlorophyceae, or filamentous bacteria that promote micritic, porous textures such as tubules, shrubs, and laminated microbialites (Freytet and Verrecchia, 2002; Pedley et al., 2009; Gandin and Capezzuoli, 2014). Abiotic precipitation, in contrast, results from CO_2 degassing in oversaturated fluids, producing sparitic calcite or aragonite with radial, bladed, or fibrous fabrics (Chafetz and Folk, 1984; Braissant et al., 2003; Pentecost, 2005). In fact, most deposits lie along a continuum between these end-members (Ford and Pedley, 1996).

Fluid sources are differentiated primarily by carbon isotope values, where surface-derived waters are enriched in organic carbon and typically produce depleted $\delta^{13}\text{C}$ values, while deeply sourced fluids interacting with carbonate bedrock or magmatic CO_2 are typically enriched (Pentecost and Viles, 1994). Sr/Ba ratios further constrain the lithologies involved in fluid pathways (Teboul et al., 2016), and $\delta^{18}\text{O}$ variations may reflect recharge regimes, residence times, or temperature-dependent water–rock interaction.

The chronological framework is established using U-Th isochron dating, which compensates for detrital contamination by resolving initial ^{232}Th through regression of coeval subsamples (Luo and Ku, 1991; Ludwig, 2003). This method is well-suited for tufa and travertine, commonly “dirty carbonates” with high detrital input, and has yielded reliable age estimates in such systems (Kaufman and Broecker, 1965; Lin et al., 1996; Garnett et al., 2004).

Against this background, the Vedi carbonates offer a unique opportunity to investigate how tectonically and volcanically influenced spring systems record hydroclimatic variability during the Middle Pleistocene. By combining petrographic, geochemical, isotopic, and geochronological tools, we reconstruct the origin and transformation of these deposits and assess their potential as paleoenvironmental archives in an under-explored part of the southern Caucasus.

2. Geological settings

The study site is located within the Ararat Depression, which has undergone a complex (and debated) tectonic history since the late Cretaceous (Avagyan et al., 2018), and is considered today one of the most active tectonic deforming regions in the world (Bozkurt, 2001). The site is located along the Vedi Fault, one of a series of NW-SE parallel faults developing as a result of the collision between the Eurasian and Arabian plates, which has resulted in the formation of depressions such as the Ararat (Fig. 1a; Avagyan et al., 2018). The Vedi Fault is situated on the eastern flank of the Erakh anticline, which is comprised of Mesozoic and Cenozoic sedimentary and volcanoclastic series (Fig. 1b).

Locally, the studied sediments are associated with a low scarp (Fig. 2b), probably representing the W-E orienting and north-dipping Vedi Fault that was suggested to be active within the radius of the study site during the late Quaternary. This stress is evidenced by deformed Holocene colluvial and debris flows (Morino et al., 2013) and dislocated and disfigured Quaternary carbonates (Karakhanyan et al., 2016). These deformed Quaternary deposits, widespread on both sides of the Vedi Valley (Fig. 1b), could share a genetic link. The studied site is part of $\sim 0.4 \text{ km}^2$ of carbonate body, located at the western end of the Vedi River floodplain (Fig. 2a–c). It comprises part of a 250 m thick sequence of Plio-Quaternary fluvial, lacustrine, and volcanic deposits (Avagyan et al., 2018).

3. Materials and methods

3.1. Field mapping, coring, and water sampling

The spatial extent of the travertine system deposits in the Vedi Valley and associated Quaternary deposits was mapped and their lithofacies were described from exposures in two quarries, excavated into a series of $\sim 5 \text{ m}$ steps (Fig. 2). Three 10 m long cores were drilled by a Geoprobe™ on three of the quarry steps, amounting to $\sim 30 \text{ m}$ long, mostly continuous cores with $>90\%$ recovery. The core was sliced open, and each portion of the core was scanned using a tabletop scanner (high-resolution images are presented in the Supplementary data). Spring water was sampled just above the quarry (Fig. 2a–c) where there are eight distinct fountain points, and each was sampled into a 4 mL vial capped with Polyseal™ screw caps.

3.2. Thin section petrography

The petrography of thirty thin sections sampled from the different facies was studied using an Olympus BX53 (Olympus Corporation, Tokyo, Japan) under Plain Polarized Light (PPL) and Crossed Polarized Light (XPL). Work scheme and characterization followed Verrecchia and Trombino (2021) by inspecting the pattern of the voids, aggregates, and microstructures as well as the fabric, including macro structures and minerals, fossils, and organic phases.

3.3. Geochemistry

3.3.1. Carbonate deposits

To evaluate the chemical composition of the carbonate deposits, we sampled the core in chosen locations (Fig. 3). Geochemical analyses were conducted by ALS Life Sciences (Dublin) using two complementary digestion protocols: four-acid digestion and lithium metaborate fusion followed by acid dissolution. Trace elements (Ba, Sr, Th, Ti, U, V, Y, Zr) were measured by ICP-MS following lithium metaborate fusion and dilute nitric acid dissolution. Major elements (Si, Fe, Al, Ca, Mg, Na, K, Cr, Ti, Mn, P, Sr, Ba) were determined by ICP-AES after the same fusion and acid procedure. In addition, base metals (Cu, Ni, Zn) were analyzed by ICP-AES following a separate four-acid digestion (HF, HNO_3 , HClO_4 , HCl). Measurements were monitored by AMIS0343, MRGeo08, OREAS 602b standards.

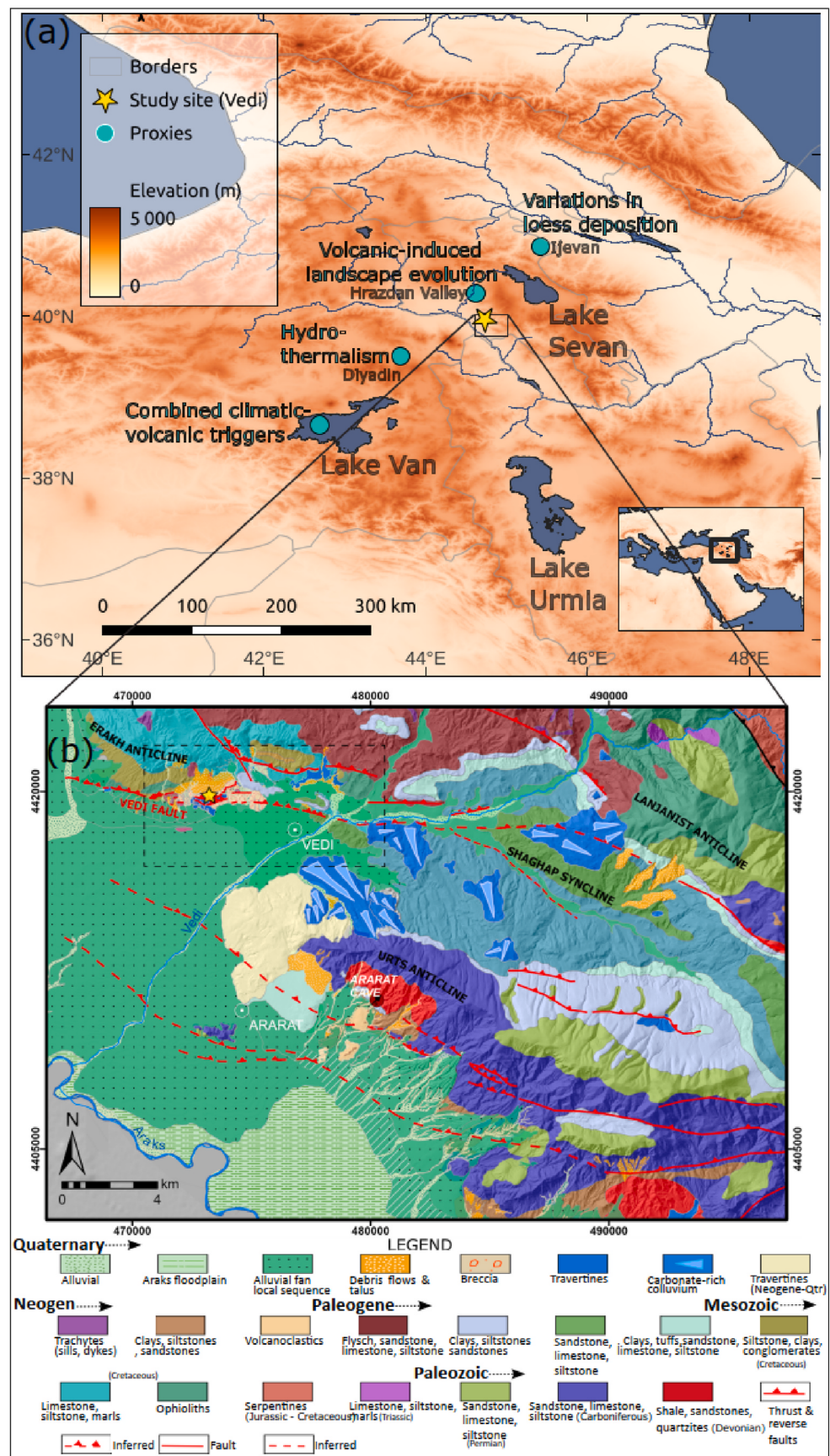
3.3.2. Spring water

Major and minor element analyses of the spring water were carried out using an inductively coupled plasma mass spectrometer (ICP-MS; Agilent 7500cx) at the Institute of Earth Sciences, Hebrew University of Jerusalem. Each sample of 0.08 mg was diluted with 5 mL of 1% HNO_3 to meet the detection limits of the ICP-MS. Calibration of the ICP-MS was performed using the MERCK VI multi-element standard.

An internal standard, comprising Sc, Rh, and Re, was added in-line to all standards and samples to correct for drift and matrix effects. Accuracy was verified using two standard reference materials: the USGS standard reference samples T-201 and T-209. The uncertainty associated with the results is 5%, and a blank correction of 0.1 ppm (1% HNO_3) was subtracted from the results to ensure accuracy.

3.4. Carbon and oxygen isotopes

Fifty-seven samples at regular intervals of 0.5 m were analyzed for carbon and oxygen stable isotopic ratios. For each sample, 0.2 g of material was drilled out of the core using a Dremel™ tool. Isotope analysis were conducted at the Environmental Isotope Lab at the University of Arizona using an automated carbonate preparation device (KIEL-III) coupled to a gas-ratio mass spectrometer (Finnigan MAT 252). Powdered samples were reacted with dehydrated phosphoric acid under vacuum at 70 °C. The isotope ratio measurement is calibrated based on



(caption on next page)

Fig. 1. (a) Elevation map of the Lesser Caucasus with locations of regional proxies mentioned in the text. Inset shows the location around the Arabian-Eurasian plate boundary. (b) geological map of the northern Ararat Depression after Avagyan et al. (2018) and Karampaglidis et al. (2025). The yellow star marks the study site. The dashed rectangle refers to the extent of Fig. 2a. (For interpretation of the references to colour in this figure legend, the reader is referred to the Web version of this article.)

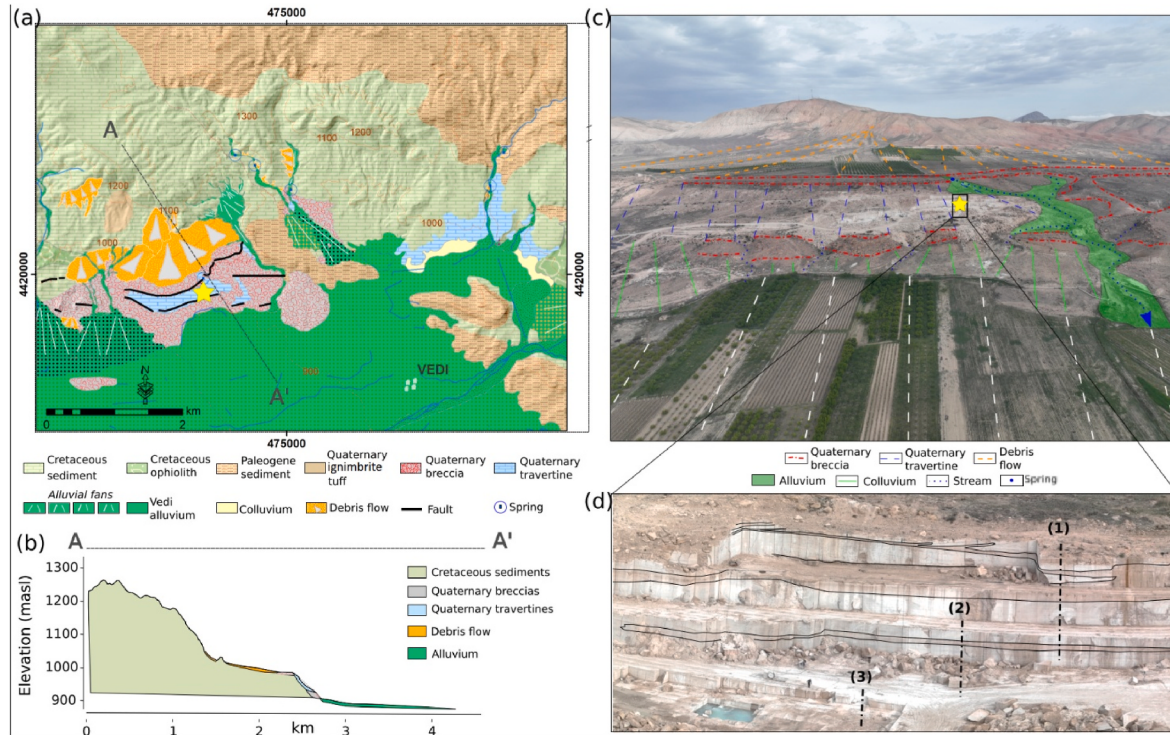


Fig. 2. (a) Geological map of the study area with the study site indicated with a yellow star. The extent of the map corresponds to the dashed rectangle in Fig. 1b. (b) Cross section of the dashed line marked A-A' in (a). (c) Drone image of the study area looking to the NW. (d) Drone image of the drilling site with core locations and highlighted field relations between two notable units. (For interpretation of the references to colour in this figure legend, the reader is referred to the Web version of this article.)

repeated measurements of NBS-19 and NBS-18, with precision of $\pm 0.11\text{‰}$ for $\delta^{18}\text{O}$ and $\pm 0.08\text{‰}$ for $\delta^{13}\text{C}$ (1σ).

3.5. Uranium series dating

We assess the ability to apply U/Th dating to the “dirty carbonates” in two locations, to provide a general time frame of deposition. Thus, isochron dating is assigned on the top and bottom of the 30 m core. Two ten cm-long sections at the top and bottom of the core were drilled in five locations. U-Th disequilibrium ages were calculated using the isochron method due to initial thorium (Luo and Ku, 1991; Haase-Schramm et al., 2004). Isochron slope, intercept, and their uncertainties were estimated after York regression (York et al., 2004) and propagated by a Monte-Carlo model.

Powdered samples (50–100 mg) were collected using a DremelTM from a freshly cut surface cleaned with deionized water. After transferring to TeflonTM vials and adding a ^{233}U - ^{236}U - ^{229}Th spike, powdered samples were dissolved in 7 N nitric acid and 0.1 N hydrofluoric acid for 24 h on a hot plate set to 150 °C. Evaporated samples were brought back up in 5 mL of 3N nitric acid. Then, 250 μL was removed for ICP-MS measurements. The remaining samples were added to an anion exchange column with 2 mL of Bio-Rad AG 1X8 200–400 mesh resin. The resin was cleaned with 6 N-HCl, <18.2 MΩ water, and then preconditioned twice with 2 mL 7 N HNO₃. After loading the samples onto the columns, Th was first eluted using 6 N HCl, and U was eluted using 1 N HBr. Both fractions were then dried and re-dissolved in 0.1 N HNO₃.

The U and Th splits eluted from the anion exchange columns were analyzed separately via a MC-ICP-MS at the Weizmann Institute of

Science. ^{238}U , ^{236}U , ^{235}U , and ^{233}U were measured on Faraday cups with: $10^{13}\Omega$ resistors for ^{236}U and ^{233}U , and a $10^{11}\Omega$ resistor for ^{238}U , and ^{235}U . ^{234}U was measured on a Daly detector with an RPQ filter. Mass fractionation of U isotopes was corrected to a $^{238}\text{U}/^{235}\text{U}$ atomic ratio of 137.88 using the exponential mass fractionation law. The multiplier-Faraday gain was calibrated using IRMM-184 measured between samples. During analysis, Faraday cups were set to half masses (234.5, 235.5, and 236.5) to correct for the influence of peak tailing on the atomic counts. The $^{234}\text{U}/^{238}\text{U}$ external 2σ standard deviation is 0.1 %. ^{229}Th and ^{230}Th were measured simultaneously on Daly detectors, and ^{232}Th was measured on a Faraday cup with a $10^{11}\Omega$ resistor. Mass fractionation of Th isotopes was corrected to the $^{238}\text{U}/^{235}\text{U}$ atomic ratio of 137.88 using the exponential mass fractionation law after spiking with the IRMM-184 standard. The gain correction was done by bracketing the samples with an IRMM-035 $^{230}\text{Th}/^{232}\text{Th}$ standard.

4. Results

4.1. Field mapping and core description

The study site is in a quarry where various freshwater carbonates of 35–40 m in thickness have been identified (Fig. 2d and 3). Detailed geological mapping of Quaternary sedimentary units in the Vedi Valley shows deposition by travertine-system in a structural scarp of approximately 50–60 m, which separates a polygenetic surface covered by debris deposits from the Ararat Depression (Fig. 1). At the base of the escarpment, breccias composed of Cretaceous gravels with red and greenish siltstones and strongly cemented carbonate matrix are

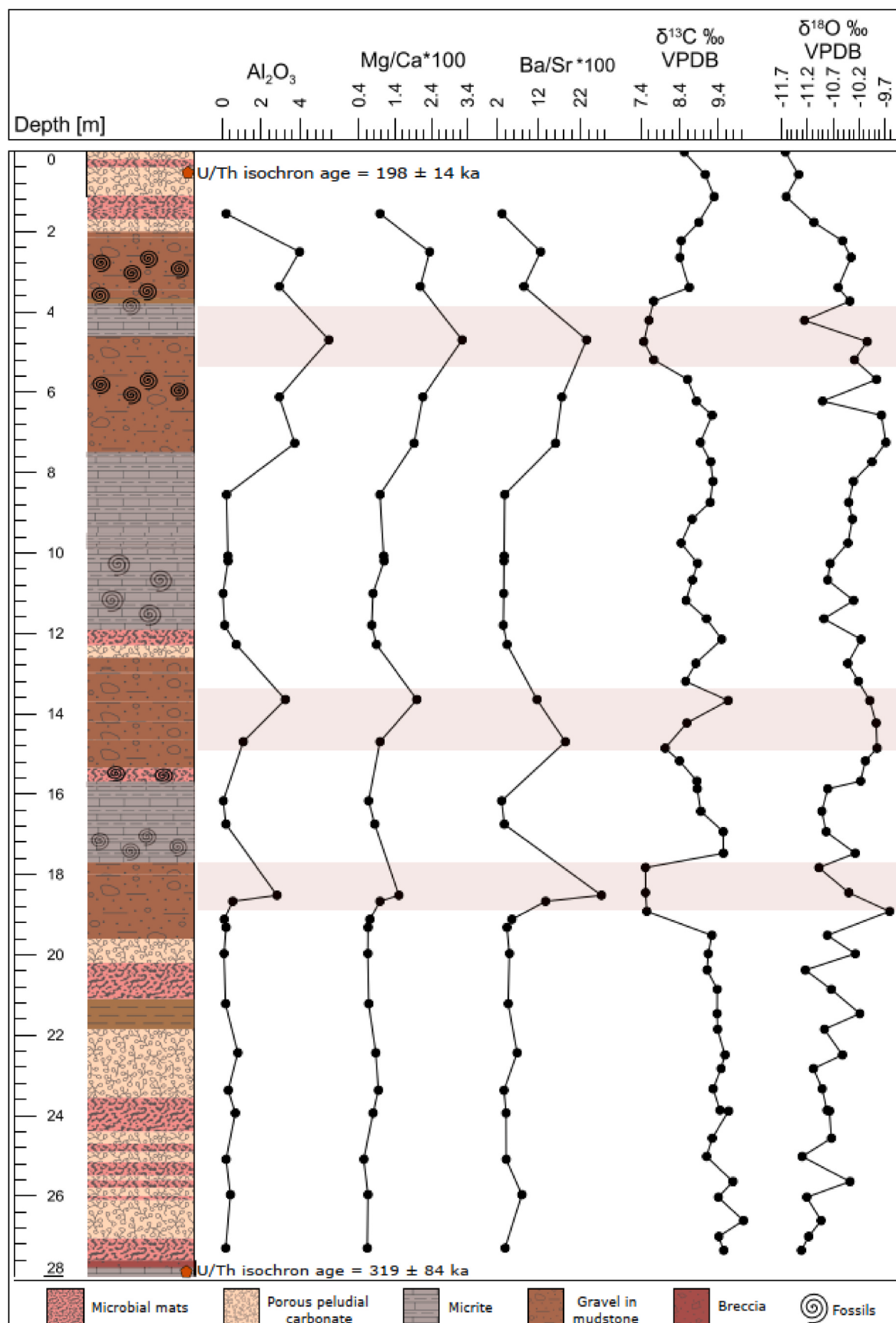


Fig. 3. Composite columnar section of carbonate deposits in the Vedi Valley, including their geochemical proxies indicative of detrital contribution and stable isotope ratios. Two U-series isochron dates are shown at the base and top of the sequence. Horizontal pink bars represent areas of significant detrital input. (For interpretation of the references to colour in this figure legend, the reader is referred to the Web version of this article.)

observed (Fig. 3), reaching ~40 m in thickness. The section exhibits sedimentological variations that reflect dynamic geothermal and meteoric fluxes, inferred from different types of fabrics that show disordered solute and sediment input (Supplementary data).

The dominant lithotype comprises palustrine micritic carbonates

associated with biological mediation and minor pedogenic alteration (Fig. 4). They preserve pristine micrite carbonate, which is present in peloidal structures (Fig. 4a and b) that were described as indicative of calcification of bacterial cells, sheaths and biofilm, and from phytoplankton-stimulated whiting nucleation (Riding, 2000). Clotted

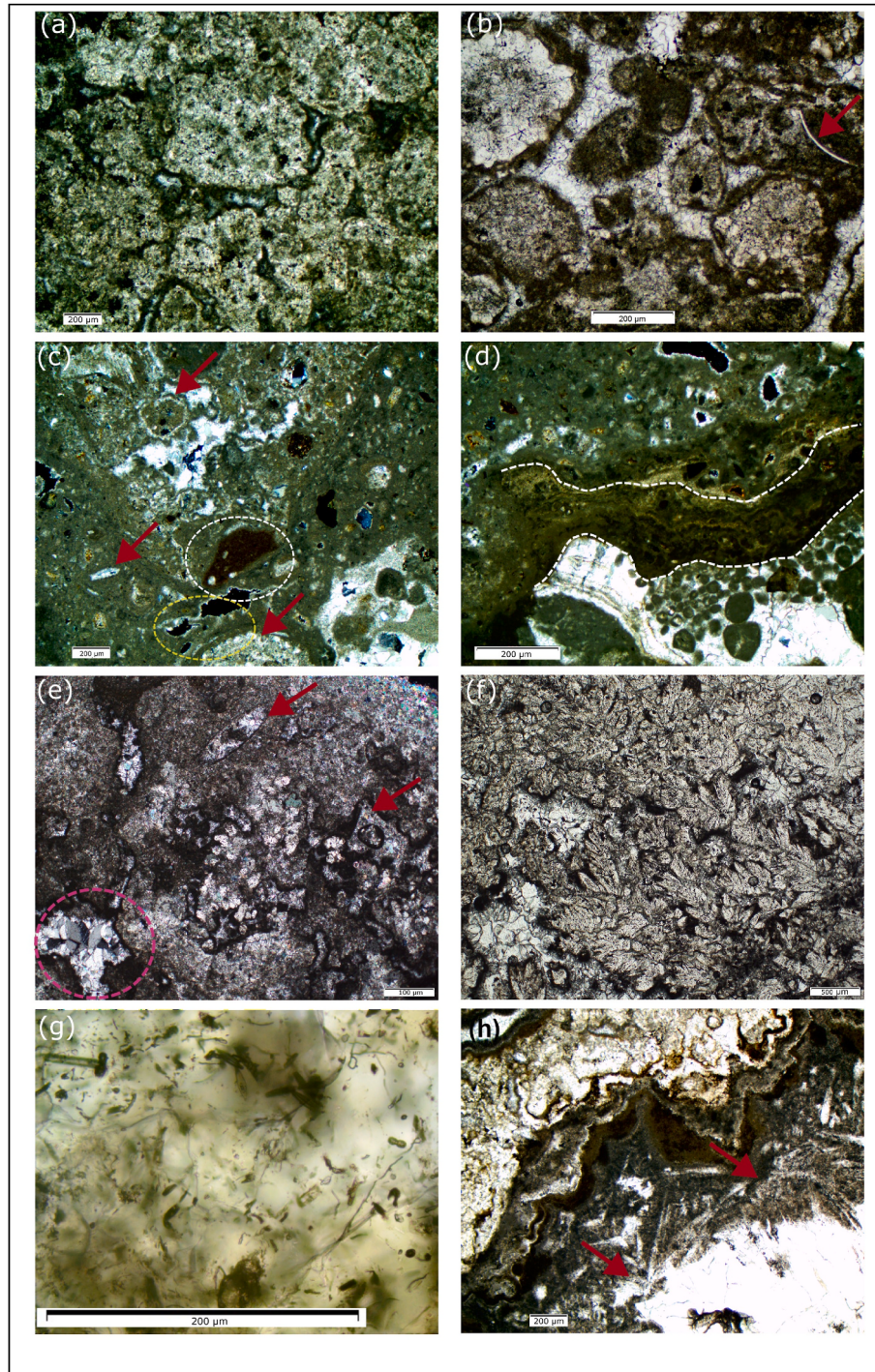


Fig. 4. Ambient palustrine deposits. (a) (XPL, 3.3 m depth) - primary growth of peloidal structures., (b) (PPL, 11.6 m depth) - remains of ostracod tests in a peloidal-clotted micrite. (c) (XPL, 3 m depth) - soil concretions and sparite filling in fossils (arrows), dissolution patterns (outlined yellow), and a variety of angular clasts, including from fossil-rich lacustrine environment (outlined white). (d) (XPL, 3 m depth) - laminated microbial mats are comfortably deposited within the upper clastic unit while exhibiting an erosional contact with the lower clastic unit. (e) (XPL, 15.2 m depth) - early diagenetic microsparite recrystallized in macro fossils. Later sparite filling is outlined. (f) (PPL, 11.7 m depth) - dendritic microsparitic structures usually form on the surface of actively evaporating and cooling still water. (g) (PPL, 1.5 m depth) - submerged environment with rich microfossil assemblage. (h) (PPL 2.2 m depth) - microbial laminated mats next to a clotted texture resembling micritized aragonite (arrows), in association with bright sparite crystals. (For interpretation of the references to colour in this figure legend, the reader is referred to the Web version of this article.)

peloids and calcareous tubules are often dark and bristling (Fig. 5 f, g, h) possibly due to bacterial remains (Freytet and Verrecchia, 2002).

The biologic felt (Forel, 1901; Freytet and Verrecchia, 2002) is composed of Chlorophyceae and Cyanobacteria fixed on rooted or floating plants and on littoral zone sediments, by filamentous bacteria in

the deeper waters, and on emerged sediments when they are not covered by phanerogams. This lithotype shows distinct porous, spongy layers with crusted calcification (Supplementary data) that were formed from decayed bryophyte colonies in areas of turbulent water flow, such as waterfalls and cascades (Viles et al., 2007; Lopez et al., 2017; Suchý

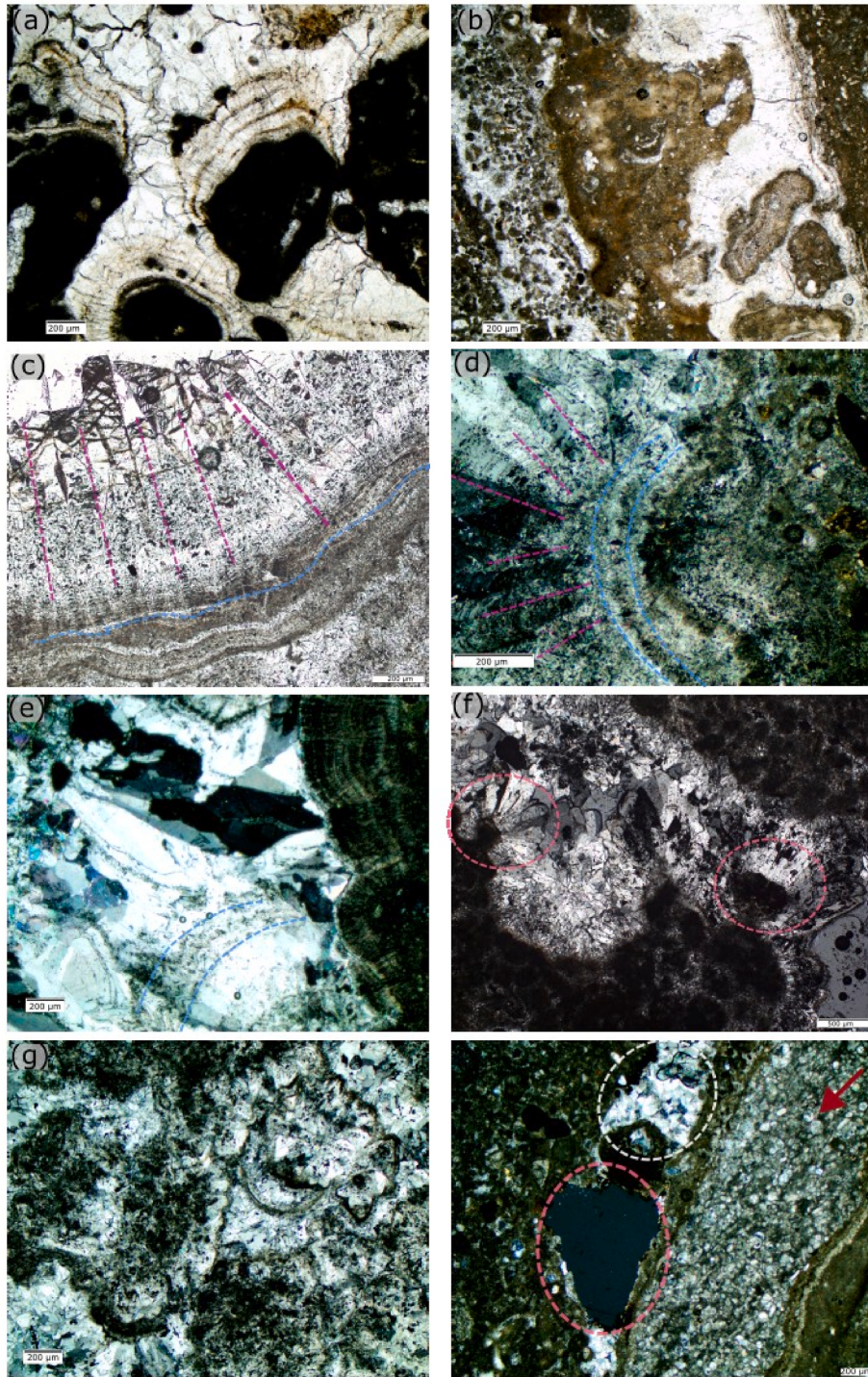


Fig. 5. Hydrothermal precipitates (a) (PPL, 3.1 m depth), (b) (PPL, 6.1 m depth) - crenulated banded layers in association with paludal facies. (c) (PPL, 9.5 m depth) - crenulated banded layers (blue) with perpendicular growth of fan ray (purple), (d) (XPL, 4.7 m depth)- sparite fan ray crystal (purple) form crenulated unconformity with microsparite deposits (blue). (e) (XPL, 3.7 m depth) - fan ray growth (left) with crenulated banded crystalline layers (blue) in association with banded layers where microsparite crystals grow perpendicular to layering (right.) (f) (XPL, 3.3 m depth) - clotted peloids and ray fan crystals (fibro radial, outlined), (g) (XPL, 5.9 m depth) clotted peloids and later sparite filling (h) (XPL, 21.6 m depth) - lacustrine clast (arrow) and dissolution patterns of in palustrine deposits (red outline). Partial sparite filling in dissolved voids is outlined white. (For interpretation of the references to colour in this figure legend, the reader is referred to the Web version of this article.)

et al., 2019). The spongy layers are associated with microbially induced sedimentary structures (MISS) (Fig. 4d,h) with both communities found in downslope areas of travertine systems, where the waters had cooled sufficiently, allowing stromatolitic tufa and bryophyte tufa to develop (Jones and Renaut, 2010). The alteration between the MISS and the bryophyte facies reflects dynamic deposition and early diagenetic processes (Viles et al., 2007; Suchý et al., 2019). These layers show in places desiccation cracks (Supplementary data) implying subaerial exposure and drying of microbial mats, and a later microsparite or sparite infilling (Freytet and Verrecchia, 2002).

A secondary lithotype is characterized by primary sparitic crystalline growth and exhibits features of active degassing from a CO₂-rich solution due to significant decompression that increases the pH, inducing precipitation of CaCO₃ (Pentecost, 2005). Such features include banded palisade crystals (onyx-like crystalline textures) (Fig. 5a, b, c) deposited by hypogene solutions filling fractures (Gandin and Capezzuoli, 2013), and fan-ray crystal growth (Fig. 5c, d, e, f, g), associated with deposition in hydrothermal systems (Mors et al., 2019). In accordance, this facies presents fibrous micriticized aragonite (Fig. 4h) that was also observed in areas adjacent to the feeding vents of active travertine systems (Jones and Renaut, 2010). These features are associated with the slow diffusion of CO₂ from CO₂-rich solutions and could be biologically induced or abiotically precipitated (Capezzuoli et al., 2014; Mors et al., 2019).

4.2. Geochemistry

Assuming Ca (as CaO) is predominantly present as CaCO₃ (based on petrographic observations), the results indicate CaCO₃ contents ranging from 70 % to 98 %. This suggests zones of nearly pure carbonate, and others where carbonate is diluted to 70–80 %. However, minor contributions from other Ca-bearing phases, such as feldspars or secondary gypsum, cannot be entirely excluded, especially in detritus-rich intervals where non-carbonate inputs may locally elevate bulk CaO concentrations.

The other dominant elements expressed as oxides are SiO₂ at 10 %, Al₂O₃ at 3 %, and Fe at 1–2 %. Samples enriched in Si and Al also show elevated concentrations of Cu, Ni, Sc, Zn, Ba, Th, Y, and Zr (Table 1;

Fig. 7), implying notable detrital material. The Si/Al ratio of the detrital material is between 5 and 6, irrespective of the facies.

In contrast, most of the analyzed elements are not notably enriched in modern spring waters, aside from Li, B, Na, and K (Table 2). Spring water Mg/Ca ratios range from 0.92 to 2.46, significantly lower than those in the carbonate deposits (1.7–17.4). This difference suggests limited fluid–rock interaction in modern springs, whereas the high Mg/Ca values in the deposits may reflect precipitation from older, more evolved fluids, possibly hydrothermal or sourced from confined aquifers.

4.3. Carbon and oxygen isotopes

The δ¹³C_{VPDB} values range from +7.5 to +10 ‰ and δ¹⁸O_{VPDB} values range from −9.6 to −11.6 ‰ (Table 3). Both δ¹³C and δ¹⁸O show primarily constant values around δ¹³C = +9 ‰, δ¹⁸O = −11 ‰, with three substantial isotopic shifts occurring at similar depths by both isotopic systems and correlate with high Si and Al concentrations. The positive δ¹³C indicate that the waters were most likely sourced from deep hypogene origins (Pentecost and Viles, 1994). The δ¹⁸O values are slightly depleted from the range observed in hydrothermal systems precipitating at high temperatures (−6 to −8 ‰), this could imply that precipitation occurred in a low-temp environment or mixing with meteoric waters (Pentecost, 2005; Capezzuoli et al., 2014).

4.4. Uranium series dating

Sample 1X, at the base of section (27.5 m), was sampled at six discrete spots, all within ~8 cm. Five of the samples yielded high ²³²Th, indicating that the isochron method is required for dating (Luo and Ku, 1991). One sample (1Xb) is characterized by massive secondary infill in voids and has very low ²³²Th. Therefore, this sample was not used for the isochron. The resultant samples (n = 5) yield an isochron age of 319 ± 84 ka (Fig. 3). Sample 3D, at the top of section (0.2 m depth), was sampled in five locations that also yielded high ²³²Th, requiring to apply isochron dating. One sample (3Da) with very high ²³⁰Th/²³⁴U (1.3), could reflect the opening of the system, and therefore, this sample was

Table 1
Major oxides (in weight %) and trace element concentrations (in ppm) in Vedi Carbonates.

Depth	ID	SiO ₂	Al ₂ O ₃	Fe ₂ O ₃	CaO	MgO	Na ₂ O	TiO ₂	Cu	Ni	Zn	Ba	Sr	Zr	Y	U	Th
1.56	3V1	0.59	0.2	0.1	54.1	0.63	0.05	0.01	3	4	15	24.6	761	5	0.7	0.96	0.08
2.51	3AD1	12.3	3.99	1.62	43	1.2	0.37	0.21	14	37	46	102.5	820	69	7.9	0.89	2.49
3.37	3AG1	9.1	2.94	1.19	45.1	1.12	0.2	0.14	12	31	39	60.8	716	44	4.3	0.7	1.5
4.7	3AR1	15.85	5.5	2.5	38.4	1.48	0.53	0.34	18	38	53	194	825	78	9.9	0.84	2.31
6.12	3BE1	10.75	2.94	1.26	44.4	1.14	0.4	0.16	11	27	25	145	824	44	5.4	0.95	1.67
7.27	3BM1	10.2	3.74	1.52	44.7	1.02	0.3	0.19	14	26	50	131.5	817	37	5.7	1.1	1.56
8.55	3BV1	0.75	0.22	0.12	53.3	0.62	0.05	0.02	3	8	16	30.8	792	6	1	1.54	0.11
10.08	3CF1	0.96	0.29	0.13	53	0.68	0.05	0.02	4	8	28	31.8	847	9	2.6	1.44	0.15
10.2	3CG1	1	0.3	0.14	53.2	0.69	0.06	0.02	4	9	22	31.2	839	10	2.6	1.47	0.16
11.01	3CK1	0.14	0.04	0.03	54.5	0.51	0.04	0.01	3	5	10	26.5	725	4	0.3	1.82	<0.05
11.8	3CO1	0.37	0.12	0.06	53.7	0.48	0.04	0.01	2	6	11	25.6	722	4	0.5	1.7	<0.05
12.28	3CP1	2.37	0.72	0.32	52.4	0.55	0.08	0.04	4	9	23	33.9	760	11	1.4	1.89	0.34
13.65	3CV1	9.71	3.25	1.44	44.7	1.06	0.19	0.15	16	28	67	63	542	46	4.1	0.8	1.57
14.7	3DE1	3.39	1.08	0.48	50.7	0.59	0.07	0.05	7	14	28	98.4	534	14	3.1	1.49	0.58
16.25	2J1	0.15	0.05	0.03	54.2	0.43	0.04	0.01	1	9	16	23.3	737	3	0.4	2.13	<0.05
16.25	2M1	0.53	0.19	0.08	54.4	0.54	0.05	0.01	2	10	17	25.2	667	10	0.6	1.74	0.08
18.52	2AA	9.42	2.82	1.2	44.9	0.8	0.31	0.14	12	29	27	160.5	593	36	5.2	0.92	1.53
18.67	2AB1	1.88	0.54	0.34	53.3	0.62	0.07	0.03	4	20	16	84.6	618	14	1.4	1.68	0.36
19.12	2AF1	0.32	0.1	0.05	55.1	0.46	0.04	0.01	2	6	14	27.4	487	4	0.9	1.63	0.08
19.31	2AG1	0.68	0.2	0.1	54.2	0.42	0.05	0.01	2	11	15	26.4	596	5	0.6	2.26	0.16
19.97	2AM1	0.3	0.09	0.05	54.7	0.42	0.03	0.01	1	11	12	26.7	530	3	0.4	1.82	<0.05
21.22	2AS1	0.53	0.17	0.08	54.1	0.43	0.04	0.02	2	14	25	24.9	525	4	0.7	1.68	0.1
22.44	2BB1	2.85	0.8	0.34	52.6	0.54	0.09	0.05	4	24	33	40.2	583	13	1.8	1.88	0.48
23.37	2BF1	1.05	0.31	0.15	53.1	0.59	0.05	0.02	2	18	19	21.1	566	9	0.8	1.36	0.18
23.94	1A	2.6	0.67	0.28	53.3	0.5	0.09	0.04	4	14	20	26.4	626	12	1.9	1.62	1.01
25.1	1I	0.74	0.2	0.08	55.1	0.35	0.02	0.01	2	14	24	19.1	449	9	1	0.84	0.14
25.97	1O	1.5	0.42	0.19	54.4	0.42	0.03	0.02	3	16	19	40.1	500	10	1.2	1	0.31
27.3	1W	0.64	0.18	0.07	54.6	0.41	0.03	0.01	2	13	15	27.1	681	6	0.4	1.47	0.12

Table 2

Major and trace element concentrations (in ppb) in spring water at the study site.

ID	Al	K	Ca	Mg	Li	B	V	Cr	Ni	Cu	Zn	As	Sr
AS 1	7	7678	17040	42002	46	9478	0.89	0.72	2.17	0.80	0.43	0.48	1184
AS 2	7	7382	18665	32648	42	8142	0.16	0.83	1.94	1.59	0.50	1.11	1325
AS 3	11	3246	13249	12584	38	9225	0.78	0.77	2.20	1.60	0.42	2.75	268
AS 4	4	13036	36981	52861	69	6077	2.46	1.00	5.72	2.84	0.28	4.27	2188
AS 5	7	6565	38132	29169	37	8553	3.96	0.86	2.53	1.53	1.19	2.75	1973
AS 6 a	4	13554	44164	59344	80	8472	1.35	0.80	2.55	0.85	0.59	4.28	2842
AS 6 b	7	8032	39995	36714	49	7074	0.9	0.87	3.41	1.54	0.81	2.98	2094
AS 6 c	4	11876	44815	44639	78	8945	6.2	0.86	3.66	2.39	0.91	3.79	2456

Table 3

Carbon and oxygen isotopic ratios.

Depth [m]	$\delta^{13}\text{C}$ ‰	±	$\delta^{18}\text{O}$ ‰	±	Depth [m]	$\delta^{13}\text{C}$ ‰	±	$\delta^{18}\text{O}$ ‰	±
0.2	8.52	0.01	-11.63	0.05	14.86	8.02	0.02	-9.85	0.04
0.58	9.06	0.01	-11.37	0.09	15.17	8.40	0.02	-10.08	0.06
1.13	9.29	0.03	-11.61	0.09	15.68	8.84	0.01	-10.17	0.04
1.77	8.89	0.01	-11.08	0.05	15.87	8.85	0.02	-10.81	0.02
2.23	8.44	0.09	-10.52	0.06	16.43	8.94	0.01	-10.92	0.04
2.65	8.41	0.01	-10.36	0.08	16.93	9.52	0.03	-10.84	0.02
3.39	8.65	0.02	-10.60	0.07	17.47	9.53	0.03	-10.27	0.09
3.74	7.73	0.02	-10.38	0.07	17.83	7.51	0.01	-10.98	0.04
4.21	7.60	0.01	-11.26	0.02	18.45	7.52	0.01	-10.40	0.03
4.74	7.47	0.02	-10.04	0.03	18.92	7.55	0.01	-9.61	0.07
5.19	7.73	0.01	-10.29	0.07	19.51	9.23	0.01	-10.81	0.04
5.68	8.60	0.08	-9.86	0.07	19.97	9.14	0.02	-10.27	0.01
6.22	8.83	0.04	-10.91	0.06	20.38	9.11	0.01	-11.24	0.07
6.57	9.24	0.02	-9.77	0.06	20.86	9.37	0.02	-10.74	0.06
7.25	8.93	0.01	-9.68	0.05	21.46	9.37	0.01	-10.19	0.01
7.73	9.20	0.02	-9.95	0.04	21.85	9.38	0.02	-10.87	0.06
8.22	9.26	0.02	-10.31	0.03	22.49	9.57	0.03	-10.52	0.04
8.74	9.18	0.02	-10.40	0.11	22.83	9.47	0.01	-11.08	0.06
9.16	8.72	0.05	-10.33	0.06	23.33	9.26	0.03	-10.91	0.02
9.75	8.44	0.01	-10.42	0.05	23.87	9.44	0.03	-10.82	0.04
10.26	8.86	0.01	-10.76	0.03	23.89	9.66	0.03	-10.77	0.03
10.67	8.73	0.01	-10.81	0.04	24.56	9.24	0.05	-10.73	0.02
11.18	8.57	0.01	-10.31	0.02	25.02	9.09	0.03	-11.30	0.05
11.64	9.09	0.01	-10.88	0.03	25.64	9.77	0.03	-10.38	0.03
12.15	9.48	0.02	-10.16	0.04	26.03	9.40	0.03	-11.21	0.03
12.75	8.82	0.03	-10.42	0.00	26.61	10.05	0.01	-10.93	0.01
13.19	8.55	0.01	-10.21	0.07	27.01	9.41	0.01	-11.17	0.01
13.67	9.65	0.02	-9.99	0.08	27.35	9.54	0.02	-11.31	0.10

not used in the isochron. The resultant samples ($n = 4$) give an isochron age of 198 ± 14 ka (Fig. 3). These ages indicate that the 30 m Vedi deposits accumulated over ~ 100 ka, resulting in a sedimentation rate of ~ 0.3 mm/yr. This sedimentation rate is slow with respect to typical travertine deposits (10–50 mm/yr, Claes et al., 2015), but within the documented range of tufa sedimentation rates (0.2–36 mm/yr; Gradiński, 2010).

5. Discussion

5.1. Depositional environments

The Vedi carbonates display two carbonate phases that formed in distinct depositional environments. The primary phase was deposited in a palustrine environment accumulating organic-rich calcareous mud and varieties of spheroidal and clotted carbonate particles (Fig. 4a and b). It preserves microbially-mediated layers with alternating finely bedded MISS and bryophyte-dominated porous layers that imply their growth and decay cycles (Gradiński, 2010). Deposition in pools and ponds probably allowed degassing at the air-water interface and cooling, leading to the settling of calcite rafts (Mors et al., 2019) and dendritic morphologies (Fig. 4f; Camuera et al., 2014). Deposition probably took place in microenvironments such as cascades, perched springlines, and dams, which are prominent niches for clast-poor deposits to accumulate in association with crystalline crusts and dendritic shrubs

(Supplementary data) (Pedley et al., 2003; Capezzuoli et al., 2014; Mors et al., 2019). The first carbonate phase also exhibits paludal stages through clast-rich layers with angular claystone and lacustrine limestone fragments. These are episodes of enhanced detrital input, evident from the lithology and geochemistry (discussed below). Early diagenesis features are apparent in the first type, including: a) cementation of microstromatolite fragments, clots, and peloids (Fig. 4b, c, d, 5h; Freytet and Verrecchia, 2002), b) crystal growth and microsparite void filling and recrystallization of shells (ostracods, gastropods, Fig. 4e), and c) dissolution patterns (Fig. 5h). Recrystallized features and erosional surfaces are associated with deposits of the second type (Fig. 4d–h, 5e), allowing multiple phases of deposition, fluid influx, and diagenetic alteration.

The secondary carbonate phase is comprised of sparite crystals that are pervasively developed across all micritic matrix by infilling veins, pores, and dissolution cavities. The formation of this phase was controlled by the decompression of hypogean solutions, as it is characterized by features reflecting fast CO₂ degassing from supersaturated solutions. Isopachous and euhedral bladed sparite crystals (Figs. 4 and 5) suggest formation within a phreatic realm, while bended palisade crystals (Fig. 5a, b, c), fan-ray crystals (Fig. 5c, d, e, f, g), and fibrous aragonite structures (Fig. 4h) are characteristic of travertine systems and often observed near vent areas (Gandin and Capezzuoli, 2014; Lopez et al., 2017; Mors et al., 2019). The presence of aragonite can indicate temporal changes, including periods of high Mg/Ca in the precipitating

solution, and is generally linked to waters that have reached high levels of supersaturation with respect to CaCO_3 . Aragonite micritization probably reflects post-degassing diagenesis by microbial filaments or boring cyanobacteria or fungi (Jones and Renaut, 2010; Camuera et al., 2014).

Finally, the long-term accumulation rate, averaging $\sim 0.3 \text{ mm/yr}$, is governed by the major (micritic) facies, suggesting dominant palustrine settings. This rate falls within the lower range of accumulation rates reported for calcareous tufa and is markedly lower than rates of $>10 \text{ mm/yr}$, typically reported for high-discharge travertine systems. This supports the interpretation of a low-intensity carbonate accumulation in low-energy freshwater systems, possibly under semi-stable hydrological conditions, such as distal spring-fed deposits with subdued flow and limited degassing (Capezzuoli, 2013). This aligns with the concept of a "travertine system" that embraces a variety of deposits sourced from a hydrothermal spring, including both travertine and tufa. The classification of such systems is not restricted to a specific temperature, especially in settings where thermal waters cool downstream, leading to deposits with mixed characteristics (Mors et al., 2019).

5.2. Sources of precipitating solutions

5.3. Geochemistry and fingerprints of the precipitating solution

5.3.1. Hypogean-epigean interplay

Geochemical and isotopic ratios can pinpoint the provenance of the solutions from which the carbonates were precipitated and the interactions between meteoric waters, deep-geothermal fluids, and lithology (Fig. 6a). The highly positive $\delta^{13}\text{C}$ of the carbonates ($+9 \text{ ‰}$) indicate a hypogean source of the solutions that were not affected by near-surface respiration CO_2 (Pentecost, 2005) and suggest a contribution from carbonate source rocks (Fig. 6a). The carbonate Sr/Ba ratio, used as a tracer of solution type and source rock (Fig. 6b; Teboul et al., 2016), further points to dominantly hypogean solutions formed within carbonates and evaporites, similar to the rocks comprising the Yerakh Anticline. Samples that plot closer to the ultra-mafic field are associated with detrital imprint (Fig. 6b). The geochemical and isotopic compositions overlap with hot-spring travertines from Tunisia that formed along faults, where the accommodating rocks include marls, limestones, clays, dolomites, and evaporites (Teboul et al., 2016). Thus, the isotopic and geochemical composition of the carbonates points to a hypogean origin of the source water, which interacted with sediments and limestones of the Yerakh Anticline, forming on the hanging wall of the Vedi Fault. This

indicates that the uplifted block to the north of the fault is the most plausible source for the solutions feeding the ancient springs in Vedi.

5.3.2. Geochemical components of carbonates and spring water

The lithological, geochemical, and isotopic data collectively reveal alternating phases of carbonate precipitation under varying degrees of detrital input (Fig. 3). Detrital-rich units exhibit a twofold enrichment in Al, Si, and Mg, and a tenfold increase in Ba/Sr ratios compared to clean carbonate intervals, indicating enhanced allochthonous contributions. These shifts are accompanied by systematic isotopic differences where $\delta^{13}\text{C}$ values are $\sim 2 \text{ ‰}$ lower in detrital-rich layers, consistent with incorporation of soil-respired CO_2 , while $\delta^{18}\text{O}$ values are $\sim 1.5 \text{ ‰}$ higher, suggesting increased influence of cooler, epigean waters.

Principal component analyses were applied on log-transformed and standardized elemental concentrations to provide insights into the sources, mixing, and evolution of deposition. We performed three different PCA analysis where one includes seven common elements in all the carbonate samples and waters (Fig. 7c), and the other two on deposits major elements (Fig. 7a) and deposits minor elements (Fig. 7b). The PCA main pole (PC1) of all samples separates the modern spring water from the sediment samples (Fig. 7c), suggesting a shift in the composition of precipitating solutions from past groundwater-dominated precipitation to present-day meteoric-influenced hydrology, as speculated for spring systems (Jones and Renaut, 2010). For the major elements (Fig. 7a), PC1 clearly distinguishes between elements associated with the carbonates (Ca, Mg, Sr) and those associated with detrital material (Al, Fe, Ti). This distinction between carbonates and detrital material is also evident in PC2 of the combined carbonates and water (Fig. 7c), where clean carbonates have negative PC2 values, and detrital carbonates have positive PC2 values (Fig. 7c).

For the carbonate major elements, PC2 separates samples with high Ba and Mn (positive) and samples with high P (negative). This is most likely the result of higher or lower hydrothermal activity, where Ba and Mn are more likely to originate from hydrothermal waters and high P from surface waters (Kaleder et al., 2015; Teboul et al., 2016).

For the carbonate minor elements, PC1 is dominated by elements that have a high affinity to carbonates (positive PC1) and those that have a higher affinity to detrital material (negative PC1). Secondary chemical processes are captured by PC2 which is responsible for 5–11 % of the variance and is influenced by limited elemental remobilization due to water-rock interaction or secondary precipitation. Positive PC2 values such as those of Na, U, and Sr reflect element mobilization due to partial alteration. U also displays a positive PC1 (Fig. 7c), pointing to its plausible adsorption onto carbonates in oxidizing conditions and later diagenetic remobilization (Pasvanoglu, 2020). Negative PC2 values are

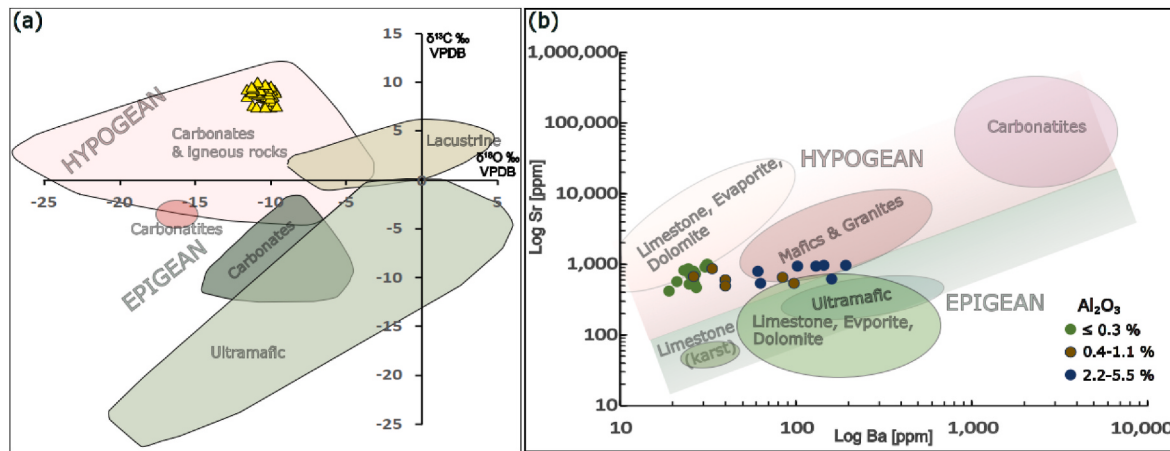


Fig. 6. Differentiating water sources using carbonate (a) $\delta^{13}\text{C}$ and $\delta^{18}\text{O}$ and (b) Sr/Ba ratios (Teboul et al., 2016). In (a), the Vedi samples are marked by yellow triangles, concentrated at the hypogene zone. In (b), detrital-rich samples that are indicated by a higher Al content plot toward the epigean field. (For interpretation of the references to colour in this figure legend, the reader is referred to the Web version of this article.)

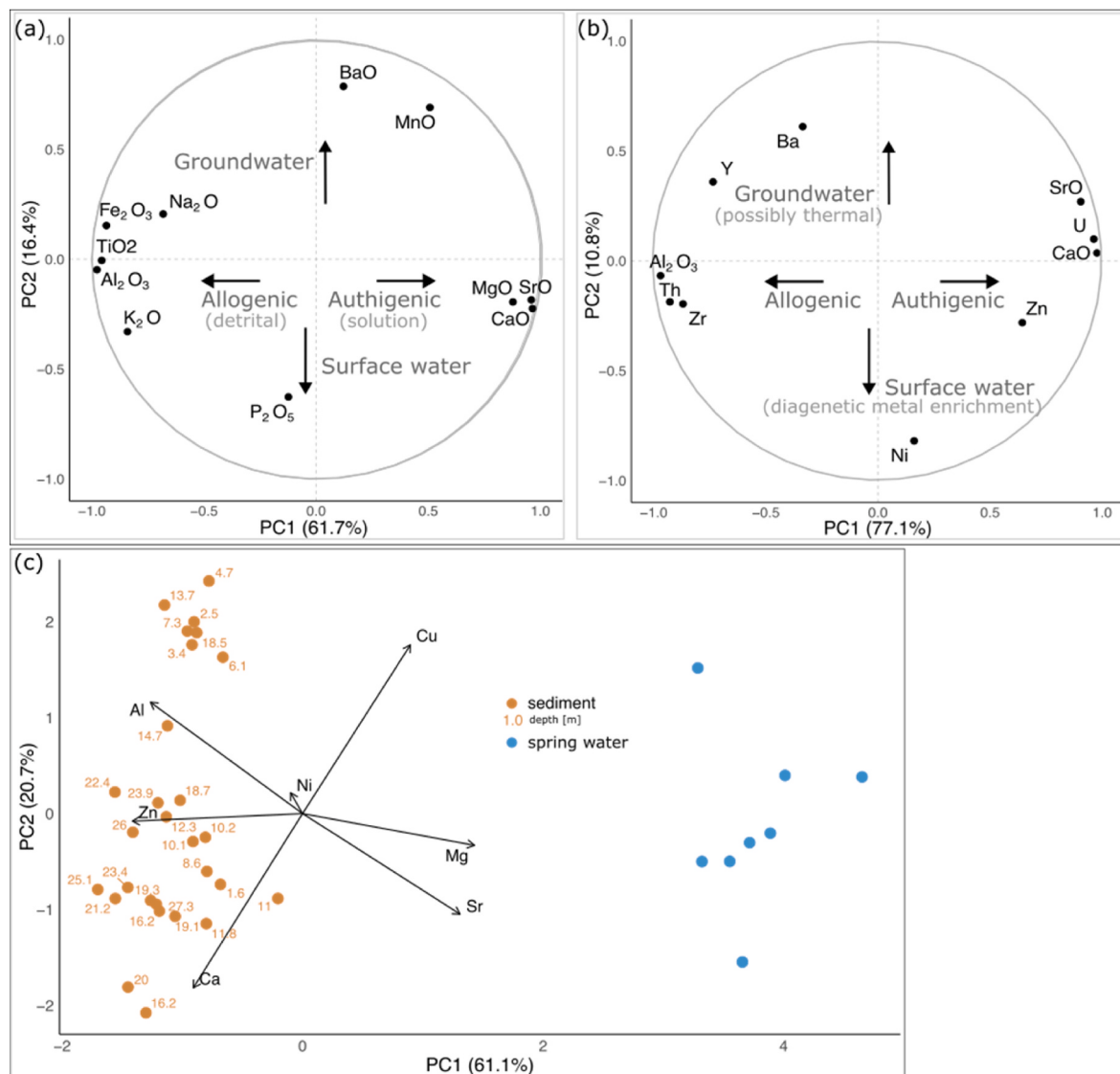


Fig. 7. Bi-plot principal component analyses of log-transformed and standardized elemental composition in Vedi carbonates and spring water. (a) shows major elements and the principal sources that affect each pole. (b) shows mostly trace elements and includes CaO, Al₂O₃, and SrO to link major and trace elements with the same sources. (c) shows a distinct variation across the main pole between the carbonate deposits and modern spring water, suggesting a change in solution composition through time.

represented by more resistant components such as Ni, Zn, Al, and K, with minor diagenetic effects, suggesting they were introduced as detrital phases and are common in siliciclastic sediments, particularly those derived from mafic rocks (Capezzuoli et al., 2014). Most neutral PC2 values characterize non-mobile elements in detrital phases including Zn, Ni, and Al, while positive values for Cu likely imply minor oxidative diagenetic Cu remobilization from detrital origin (Teboul et al., 2016).

5.3.3. Modern spring chemistry

Currently, the site experiences the flux of spring water at surface temperature as well as all adjacent springs in the Vedi Valley with temperatures not exceeding 21 °C (Fig. 2a c; Schubert et al., 2021). Similarly to the travertine system deposits, today's waters are not significantly enriched in Ba or trace metals such as As, Cu, Ni, Zn (Table 2) that are often enriched in hot geothermal systems where leaching is intense. This suggests that hydrothermal activity did not occur at high temperatures. Nonetheless, trace metal concentrations and elevated Li and K are consistent with groundwater under some volcanic influence, with Li concentrations corresponding to water temperatures of 20–60 °C. The enrichment of K is associated with the abundance of

feldspar in volcanic and sedimentary systems and the accompanied gases under volcanic or low-to moderate-temperature geothermal influence (Drever, 1988; Giggenbach, 1992). This could point to the contribution of weathering products from the felsic to intermediate volcanics of the Gegham Upland, which borders the Vedi Valley to the east (Karakhanyan et al., 2016; Avagyan et al., 2018).

5.3.4. Prior calcite precipitation

To evaluate whether the clean carbonates formed in a closed, open, or mixed system, we consider the covariance of $\delta^{18}\text{O}$ and $\delta^{13}\text{C}$ and the behavior of Mg and Sr during prior calcite precipitation (PCP) as assessed by $\ln(\text{Sr}/\text{Ca})$ vs. $\ln(\text{Mg}/\text{Ca})$ trends (Sinclair, 2011; Sinclair et al., 2012). In the lower 10 m, $\delta^{13}\text{C}$ and $\delta^{18}\text{O}$ covary (Fig. 3), with a gradual decline in $\delta^{13}\text{C}$ and a parallel increase in $\delta^{18}\text{O}$ of ~1 ‰. This pattern aligns with models of Rayleigh-type fractionation from a constant solution source during CO₂ degassing under closed-system conditions, where CO₂ loss drives enrichment in $\delta^{18}\text{O}$ and depletion in $\delta^{13}\text{C}$ in the residual dissolved inorganic carbon pool (Capezzuoli et al., 2014; Pentecost and Viles, 1994). These trends are supported by the stable preservation of U concentrations (1.0–2.3 ppm) and low Th (<0.5 ppm),

suggesting early entrapment under reducing conditions and minimal post-depositional alteration (Roberts et al., 1998). The highest porosity in the form of gas-escape structures, also characterizes the lower meters of the section, further supporting precipitation in a low-permeability, CO₂-saturated environment.

To assess the potential influence of PCP and detrital mixing on carbonate composition, we categorized samples based on Al₂O₃ content as a proxy for allochthonous input: poor ($\leq 0.3\%$), mixed (0.4–1.1 %), and rich (2.2–5.5 %) (Fig. 8). When plotted in ln (Sr/Ca) vs. ln(Mg/Ca) space (Fig. 8) all groups plot below the PCP line, implying primary deposition with little Mg and Sr remobilization due to diagenetic processes (Leleu et al., 2016). The Al-rich group plots further away from the PCP zone than the two low Al₂O₃ groups due to significant amounts of Mg in the epigean solution that would be enriched from nearby dolomitic and Mg-rich volcano-clastic lithologies (Lebedev et al., 2018; Karampaglidis et al., 2025). The deviation of the Al-rich samples from the PCP line could suggest an open system with episodic contributions from meteoric waters due to periods of increased runoff. Overall, the narrow Si/Al range (5–6) suggests that the origin of the detrital material is similar throughout the core and that the primary process differentiating between the types is the ratio between detrital input and carbonate precipitation rates. Thus, the lithology, chemistry, and isotopes of the Vedi carbonates point to an interplay between hypogean-sourced carbonate and detrital-rich units sourced from a mixture of hypogean and epigean waters.

5.4. Time frame and regional perspective

The U/Th ages of the Vedi carbonates (319 ± 84 and 198 ± 14 ka) indicate that they were deposited throughout MIS 9–7, a period marked by alternating global and regional climates (Fig. 9). These climatic perturbations likely impacted regional water availability, modulating the intensity and nature of deposition in Vedi. While the current chronological resolution does not allow precise constraints on the timing of

environmental changes in Vedi, its coincidences with regional observations of substantial environmental changes that occurred during the global glaciation of MIS 8 (~260 ka) (Fig. 9; Siddall et al., 2007; Litt et al., 2014). Such changes were suggested to trigger a major transition in loess-paleosol sedimentation located ~150 km to the north of Vedi (Fig. 1a).

Changes in the configuration of the geological structure and nearby volcanic activity could have also shaped the carbonate facies and geochemistry by modulating water and solute compositions. Evidence of substantial geological instabilities have been documented during the deposition time of the Vedi carbonates, these are: (1) the thrusting southwards of massive Quaternary travertine and travertine breccia over lacustrine Pleistocene deposits, ~20 km to the south of the study site (Paffenholz, 1948; Avagyan et al., 2018); (2) strike-slip movement on the western margins of the Ararat Depression that triggered the development of the Tondrak/Tendürek Volcano and the Diyadin geothermal field in the Anatolian eastern margins, <100 km from Vedi (Fig. 1a). There, travertine-system deposits that reach 200 m in thickness are intercalated with Plio-Quaternary volcanics (Koçyiğit, 2023); (3) two out of five of the most significant low stand stages at Lake Van (200 km SW of Vedi, Fig. 1a) took place at ca. 365–340 and 290–230 ka and were strongly affected by climatic shifts (Cukur et al., 2014). However, the main phase of deformation during the development of the Lake Van Basin occurred between these low stands (Cukur et al., 2017), hampering the differentiation of tectonic vs. climatic controls. After 230 ka, the environmental pattern in Lake Van deposits notably changed due to increased volcanic activity, mostly from the Nemrut Volcano that is located on the western margins of Lake Van, 250 km from Vedi (Sumita and Schmincke, 2013; Litt et al., 2014). Finally, distinct geomorphological and ecological changes are inferred from sediments in the Hrazdan Valley and pollen in Lake Van, associated with volcanic deposits (Sherriff et al., 2022; Pickarski et al., 2023).

While these regional observations demonstrate significant climatic and tectonic fluctuations, the Vedi sequence provides local evidence for

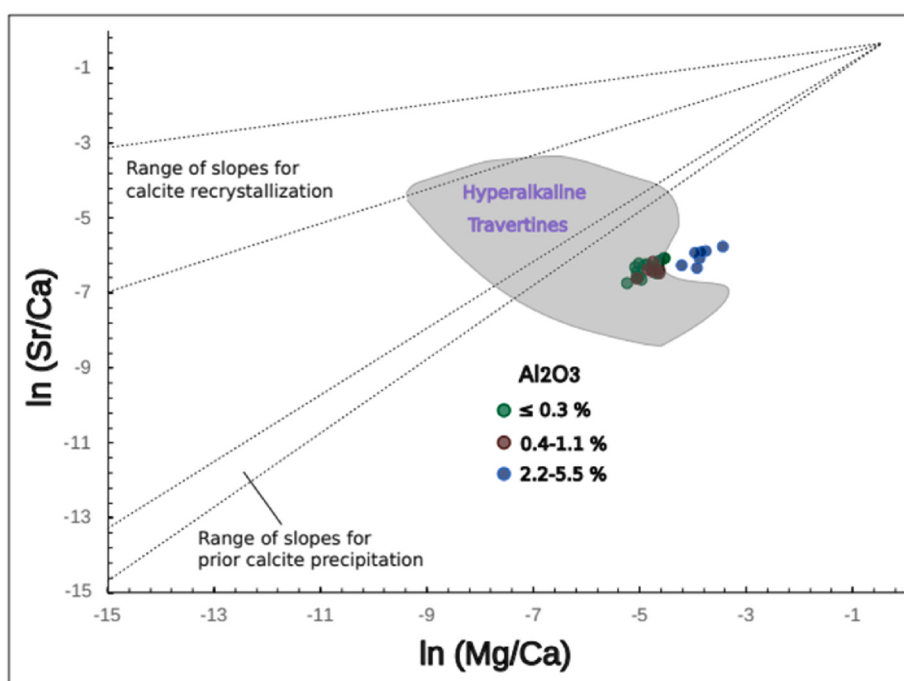


Fig. 8. Sr vs. Mg as precipitation-type predictors (after Sinclair, 2011; Sinclair et al., 2012). Typical slopes are plotted for (lower slope range)-prior calcite precipitation in a closed system where Ca is progressively removed by calcite precipitation while enriching Mg and Sr, and (upper slope range)-incongruent dissolution due to selective element release during partial dissolution in an open system. Gray polygon depicts the range of values for hyperalkaline travertine deposits in Oman (Leleu et al., 2016). The Vedi carbonates partially plot within this range, with outliers being enriched in Al₂O₃, pointing to mixing with meteoric water carrying detrital input.

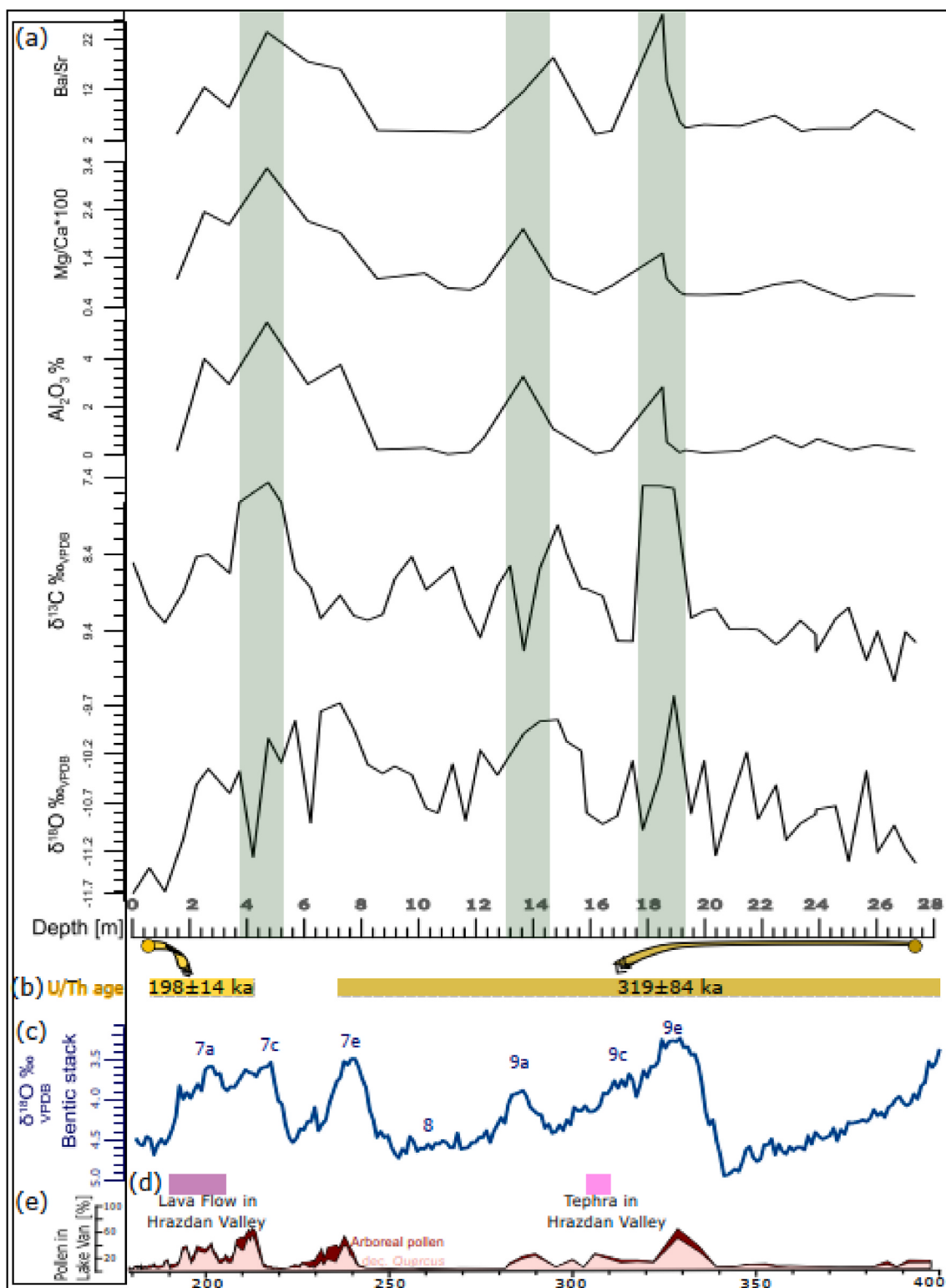


Fig. 9. (a) Stable Isotopes, Al₂O₃, Mg/Ca, and Ba/Sr ratios. Vertical green bars indicate periods of increased detrital components suggesting heightened runoff. (b) U-Th ages with confidence interval bounds in light and dark yellow. (c) the benthic stack δ¹⁸O_{PDB} and MIS (Lisicki and Raymo, 2005). (d) proximate volcanism inferred to affect depositional environments at the Hrazdan Valley (Sherriff et al., 2022). (e) the relative abundance of arboreal pollen in Lake Van which was linked with changes in climate and volcanic events (Litt et al., 2014; Pickarski et al., 2023). (For interpretation of the references to colour in this figure legend, the reader is referred to the Web version of this article.)

how such changes are reflected in carbonate deposits. Wetter climatic periods likely enhanced meteoric recharge and runoff, promoting detrital input and shifting solutions chemistry through mixing with shallow epigean waters. In contrast, arid intervals would have suppressed surface inflow, allowing relatively undiluted hypogene fluids to dominate and favor the precipitation of chemically distinct carbonates. Thus, the transition into increased input of meteoric water in the upper 20 m of the Vedi sequence could reflect the transition into the humid MIS 7e interglacial interval around 240 ka. However, tectonic activity could have additionally altered fracture permeability, fluid pathways, and upflow rates, further modulating the flux and composition of spring discharge.

6. Conclusions

The travertine-system deposits and modern spring system in Vedi are situated along a structural scarp, associated with a dense fault system within a volcanically active area. We studied a ~30 m thick section composed of different types of carbonate deposits representing the interplay between deeply sourced hydrothermal solutions and surface water.

First-order classification highlights two sedimentary facies (1) biogenic, with micritic and peloidal textures, deposited in low-energy, palustrine environments, and (2) crystalline sparite calcite facies formed due to CO₂ degassing and associated with hydrothermal activity under relatively low temperature. These deposits display overall high δ¹³C_{VPPDB} (9 ‰), reflecting the importance of hypogene source to the precipitating solution. Geochemical discrimination analyses point to carbonates as the hosting rocks under thermally low conditions, making the Yerakh Anticline, lying on the hanging wall of the Vedi Fault, the most probable ancient aquifer. While the lower 10 m are characterized by δ¹⁸O and δ¹³O coupling, indicating a closed travertine system, isotopic ratios above 19 m depth are more variable and often change with geochemical proxies, indicative of enhanced detrital input. These detrital-rich units probably resulted from increased precipitation and runoff during interglacial intervals.

Uranium-series dating places deposition between 319 ± 84 ka and 198 ± 14 ka, spanning glacial-interglacial cycles of MIS 9-7 and coinciding with regional tectonic and volcanic activity. This study demonstrates the recording of the combined effect of these processes and their effects on spring-fed deposition. Future work, including high-resolution U-series dating and selective isotopic and petrographic analyses, could clarify the timing of depositional phases and improve our understanding of the role of climatic and tectonic forces in controlling carbonate formation in tectonically active regions.

Author contributions

Shlomy Vainer: data curation, software, visualization, investigation, validation, writing original draft; Alex Brittingham: data curation, visualization, writing original draft; Theodoros Karampaglidis: data curation, software, visualization, writing original draft; Boris Gasparyan: data curation, investigation, validation; Artur Petrosyan: data curation, investigation, validation; Hayk Haydosyan: data curation; Dmitri Arakelyan: data curation; Yael Kiro: data curation, investigation, validation; Yonaton Goldsmith: data curation, software, visualization, investigation, validation, writing original draft, review & editing; Ariel Malinsky-Buller: project administration; resources; validation.

Declaration of competing interest

The authors declare that they have no known competing financial interests or personal relationships that could have appeared to influence the work reported in this paper.

Acknowledgments

The Authors would like to thank the director of the Institute of Archaeology and Ethnography of the National Academy of Sciences of the Republic of Armenia, Dr. Arsen Bobokhyan, who kindly supported the project and provided corresponding permits for transportation of the samples under the frame of the grant number 21AG-6A080 of the Higher Education and Science Committee, Republic of Armenia. We are grateful for the advice and comments brought up by Eric Verrecchia that notably improved the clarity, robustness, and validity of this article. We acknowledge the support given by Regev Hamiel, Naomi Moshe, and Ofir Tirosh. This research was supported by the Fritz-Thyssen Foundation grant awarded for the project “Pleistocene Hunter-Gatherer Lifeways and Population Dynamics in the Ararat (paleo-lake) Depression, Armenia”, and The European Research Council grant N 948015: “Investigating Pleistocene population dynamics in the Southern Caucasus” (awarded to AMB). Further support was provided by Gfoeller Renaissance Foundation (USA) and “Areni-1 Cave” Consortium (“Areni-1 Cave” Scientific Research Foundation (Armenia)), and the Institute of Archaeology and Ethnography of the National Academy of Sciences of the Republic of Armenia. We kindly thank N. Paz and the Human-Environment Dynamics Laboratory of the Institute of Archaeology, the Hebrew University of Jerusalem, for providing laboratory facilities and support during the research.

Appendix A. Supplementary data

Supplementary data to this article can be found online at <https://doi.org/10.1016/j.quascirev.2025.109596>.

Data availability

All data and/or code are contained within the submission.

References

- Alonso-Zarza, A.M., 2003. Palaeoenvironmental significance of palustrine carbonates and calcretes in the geological record. *Earth-Science Reviews* 60 (3–4), 261–298.
- Alonso-Zarza, A.M., Tanner, L.H., 2009. Carbonates in continental settings: facies, environments, and processes, 61. Elsevier.
- Andrews, J.E., 2006. Palaeoclimatic records from stable isotopes in riverine tufas: synthesis and review. *Earth-Science Rev.* 75, 85–104. <https://doi.org/10.1016/j.earscirev.2005.08.002>.
- Avagyan, A., Sosson, M., Sahakyan, L., Sheremet, Y., Vardanyan, S., Martirosyan, M., et al., 2018. Tectonic evolution of the northern margin of the cenozoic Ararat basin, lesser Caucasus, Armenia. *J. Pet. Geol.* 41 (4), 495–511.
- Bozkurt, E., 2001. Neotectonics of Turkey—a synthesis. *Geodin. Acta* 14 (1–3), 3–30.
- Braissant, O., Caillet, G., Dupraz, C., Verrecchia, E.P., 2003. Bacterially induced mineralization of calcium carbonate in terrestrial environments: the role of exopolysaccharides and amino acids. *J. Sediment. Res.* 73, 485–490. <https://doi.org/10.1306/111302730485>.
- Camuera, J., Alonso-Zarza, A.M., Rodríguez-Berriguete, Á., Rodríguez-González, A., 2014. Origin and palaeo-environmental significance of the berrazales carbonate spring deposit, north of gran canaria island, Spain. *Sediment. Geol.* 308, 32–43. <https://doi.org/10.1016/j.sedgeo.2014.04.005>.
- Capezzuoli, E., Gandin, A., Pedley, M., 2014. Decoding tufa and travertine (fresh water carbonates) in the sedimentary record: the state of the art. *Sedimentology* 61, 1–21. <https://doi.org/10.1111/sed.12075>.
- Chafetz, H.S., Folk, R.L., 1984. Travertines; depositional morphology and the bacterially constructed constituents. *J. Sediment. Res.* 54 (1), 289–316.
- Claes, H., Soete, J., Van Noten, K., El Desouky, H., Marques Erthal, M., Vanhaecke, F., Özkul, M., Swennen, R., 2015. Sedimentology, three-dimensional geobody reconstruction and carbon dioxide origin of Pleistocene travertine deposits in the Ballık area (south-west Turkey). *Sedimentology* 62 (5), 1408–1445.
- Cukur, D., Krastel, S., Schmincke, H.U., Sumita, M., Tomonaga, Y., Namik Çağatay, M., 2014. Water level changes in Lake Van, Turkey, during the past ca. 600 ka: climatic, volcanic and tectonic controls. *J. Paleolimnol.* 52, 201–214.
- Cukur, D., Krastel, S., Tomonaga, Y., Schmincke, H.U., Sumita, M., Meydan, A.F., Çağatay, M.N., Toker, M., Kim, S.P., Kong, G.S., Horozal, S., 2017. Structural characteristics of the Lake Van Basin, eastern Turkey, from high-resolution seismic reflection profiles and multibeam echosounder data: geologic and tectonic implications. *Int. J. Earth Sci.* 106, 239–253.
- Drever, J.I., 1988. The Geochemistry of Natural Waters: Surface and Groundwater Environments. Prentice Hal.

- Ford, T.D., Pedley, H.M., 1996. A review of tufa and travertine deposits of the world. *Earth-Science Rev.* 41, 117–175. [https://doi.org/10.1016/S0012-8252\(96\)00030-X](https://doi.org/10.1016/S0012-8252(96)00030-X).
- Forel, F.A., 1901. *Le Léman, Monographie Limnologique, III. F. Rouge*, p. 715. Lausanne.
- Freytet, P., Verrecchia, E.P., 2002. Lacustrine and palustrine carbonate petrography: an overview. *J. Paleolimnol.* 27, 221–237.
- Gandin, A., Capezzuoli, E., 2014. Travertine: distinctive depositional fabrics of carbonates from thermal spring systems. *Sedimentology* 61, 264–290. <https://doi.org/10.1111/sed.12087>.
- Garnett, E.R., Gilmour, M.A., Rowe, P.J., Andrews, J.E., Preece, R., 2004. $^{230}\text{Th}/^{234}\text{U}$ dating of Holocene tufas: possibilities and problems. *Quat. Sci. Rev.* 23, 947–958. <https://doi.org/10.1016/j.quascirev.2003.06.018>.
- Giggenbach, W.F., 1992. The composition of gases in geothermal and volcanic systems as a function of tectonic setting. In: *Proceedings of the International Symposium on Water-Rock Interaction*, 7, pp. 873–878.
- Gradziński, M., 2010. Factors controlling growth of modern tufa: results of a field experiment. *Geol. Soc. London, Spec. Publ.* 336 (8), 143–191. <https://doi.org/10.1144/SP336>.
- Haase-Schramm, A., Goldstein, S.L., Stein, M., 2004. U-Th dating of Lake Lisan (late Pleistocene Dead Sea) aragonite and implications for glacial East Mediterranean climate change. *Geochem. Cosmochim. Acta* 68, 985–1005. <https://doi.org/10.1016/j.gca.2003.07.016>.
- Jones, B., Renaut, R.W., 2010. Calcareous spring deposits in continental settings. *Dev. Sedimentol.* 61, 177–224.
- Kalender, L., Okan, Ö.O., İnceoz, M., Çetindag, B., Yıldırım, V., 2015. Geochemistry of travertine deposits in the eastern anatolia district: an example of the karakoçan-yoğunağac (elazığ) and mazgirt-dedebağ (tunceli) travertines, Turkey. *Turk. J. Earth Sci.* 24 (6), 607–626.
- Karakhanian, A., Arakelyan, A., Avagyan, A., Sadoyan, T., 2016. Aspects of the seismotectonics of Armenia: new data and reanalysis. In: Sorkhabi, R. (Ed.), *Tectonic Evolution, Collision, and Seismicity of Southwest Asia: in Honor of Manuel Berberian's Forty-Five Years of Research Contributions*, 525. Geological Society of America Special Paper, pp. 1–34. [https://doi.org/10.1130/2016.2525\(14\)](https://doi.org/10.1130/2016.2525(14)).
- Karampaglidis, T., Fenn, K., Gasparyan, B., Braucher, R., Lauer, T., Vainer, S., Gevorgyan, H., Arakelyan, D., Oikonomou, I., Haydosyan, H., Rogall, D., 2025. Paleolithic hominin occupations and Quaternary geomorphological evolution in the NE Ararat Depression (Armenia). *Quaternary Science Reviews* 368, 109532.
- Kaufman, A., Broecker, W., 1965. Comparison of Th 230 and C 14 ages for carbonate materials from lakes Lahontan and Bonneville. *J. Geophys. Res.* 70, 4039–4054. <https://doi.org/10.1029/JZ070i016p04039>.
- Koçyiğit, A., 2023. Neotectonic and geothermal potential of the east anatolian tectonic block: a case study in Diyarbakır (ağrı) geothermal field, ne Türkiye. *Bulletin of the Mineral Research and Exploration*, (early view), 1–1.
- Lebedev, V.A., Chernyshev, I.V., Sagatelyan, A.K., Goltsman, Y.V., Oleinikova, T.I., 2018. Miocene-Pliocene volcanism of Central Armenia: geochronology and the role of AFC processes in magma petrogenesis. *J. Volcanol. Seismol.* 12 (5), 310–331.
- Leleu, T., Chavagnac, V., Delacour, A., Noiriel, C., Ceuleneer, G., Aretz, M., Rommevaux, C., Ventalon, S., 2016. Travertines associated with hyperalkaline springs: evaluation as a proxy for paleoenvironmental conditions and sequestration of atmospheric CO₂. *J. Sediment. Res.* 86 (11), 1328–1343.
- Lin, J.C., Broecker, W.S., Anderson, R.F., Hemming, S., Rubenstein, J.L., Bonani, G., 1996. New $^{230}\text{Th}/\text{U}$ and ^{14}C ages from Lake Lahontan carbonates, Nevada, USA, and a discussion of the origin of initial thorium. *Geochim. Cosmochim. Acta* 60, 2817–2823. [https://doi.org/10.1016/0016-7037\(96\)00136-6](https://doi.org/10.1016/0016-7037(96)00136-6).
- Lisiecki, L.E., Raymo, M.E., 2005. A Pliocene-Pleistocene stack of 57 globally distributed benthic $\delta^{18}\text{O}$ records. *Paleoceanography* 20 (1).
- Litt, T., Pickarski, N., Heumann, G., Stockhecke, M., Tzedakis, P.C., 2014. A 600,000 year long continental pollen record from Lake Van, eastern Anatolia (Turkey). *Quat. Sci. Rev.* 104, 30–41.
- Lopez, B., Camoin, G., Özkul, M., Swennen, R., Virgone, A., 2017. Sedimentology of coexisting travertine and tufa deposits in a mounded geothermal spring carbonate system, Obruktepe, Turkey. *Sedimentology* 64 (4), 903–931.
- Ludwig, K.R., 2003. Mathematical-statistical treatment of data and errors for $^{230}\text{Th}/\text{U}$ geochronology. In: *Uranium-Series Geochemistry*. De Gruyter, pp. 631–656. <https://doi.org/10.1515/9781501509308-021>.
- Luo, S., Ku, T.-L., 1991. U-series isochron dating: a generalized method employing total-sample dissolution. *Geochem. Cosmochim. Acta* 55, 555–564. [https://doi.org/10.1016/0016-7037\(91\)90012-T](https://doi.org/10.1016/0016-7037(91)90012-T).
- Morino, M., Kaneko, F., Matsuo, J., 2013. *Active Vedi Fault Identified on the Northeastern Margin of Ararat Depression, Republic of Armenia, and its Significance: Active Fault Research*, 38. Japanese Society for Active Fault Studies), pp. 41–49.
- Mors, R.A., Astini, R.A., Gomez, F.J., 2019. Coexisting active travertines and tufas in the southeastern border of the Puna plateau. *Sediment. Geol.* 389, 200–217.
- Paffenholz, K.N., 1948. Geology of Armenia. *Min. Geol. SSSR*, p. 895. Moscow.
- Pasvanoglu, S., 2020. Geochemistry and conceptual model of thermal waters from Ercīz Zilan Valley, Eastern Turkey. *Geothermics* 86, 101803.
- Pedley, M., Martín, J.A.G., Delgado, S.O., García Del Cura, M., 2003. Sedimentology of Quaternary perched springline and paludal tufas: criteria for recognition, with examples from Guadalajara Province, Spain. *Sedimentology* 50 (1), 23–44.
- Pedley, M., Rogerson, M., Middleton, R., 2009. Freshwater calcite precipitates from in vitro mesocosm flume experiments: a case for biomeditation of tufas. *Sedimentology* 56, 511–527. <https://doi.org/10.1111/j.1365-3091.2008.00983.x>.
- Pentecost, A., Viles, H., 1994. A review and reassessment of travertine classification. *Géogr. Phys. Quaternaire* 48, 305–314. <https://doi.org/10.7202/033011ar>.
- Pentecost, A., 2005. *Travertine*. Springer, Berlin, p. 445.
- Pickarski, N., Kwiecien, O., Litt, T., 2023. Volcanic impact on terrestrial and aquatic ecosystems in the Eastern Mediterranean. *Commun. Earth Environ.* 4 (1), 167.
- Riding, R., 2000. Microbial carbonates: the geological record of calcified bacterial-algal mats and biofilms. *Sedimentology* 47, 179–214.
- Roberts, M.S., Smart, P.L., Baker, A., 1998. Annual trace element variations in a Holocene speleothem. *Earth Planet Sci. Lett.* 154 (1–4), 237–246.
- Schubert, M., Michelsen, N., Schmidt, A., Eichenauer, L., Knoeller, K., Arakelyan, A., Harutyunyan, L., Schüth, C., 2021. Age and origin of groundwater resources in the Ararat Valley, Armenia: a baseline study applying hydrogeochemistry and environmental tracers. *Hydrogeol. J.* 29 (7), 2517–2527.
- Sherriff, J.E., Wilkinson, K.N., Harding, P., Hawkins, H., Timms, R.G., Adler, D.S., Beverly, E.J., Blockley, S.P., Gasparyan, B., Manning, C.J., Mark, D., 2022. Middle Pleistocene environments, landscapes and tephrostratigraphy of the Armenian highlands: evidence from Bird Farm 1, Hrazdan Valley. *J. Quat. Sci.* 37 (1), 6–27.
- Siddall, M., Stocker, T.F., Blunier, T., Spahni, R., Schwander, J., Barnola, J.M., Chappellaz, J., 2007. Marine Isotope Stage (MIS) 8 millennial variability stratigraphically identical to MIS 3. *Paleoceanography* 22 (1).
- Sinclair, D.J., 2011. Two mathematical models of Mg and Sr partitioning into solution during incongruent calcite dissolution: implications for dripwater and speleothem studies. *Chem. Geol.* 283 (3–4), 119–133.
- Sinclair, D.J., Banner, J.L., Taylor, F.W., Partin, J., Jenson, J., Mylroie, J., Goddard, E., Quinn, T., Jocson, J., Miklavčič, B., 2012. Magnesium and strontium systematics in tropical speleothems from the Western Pacific. *Chem. Geol.* 294, 1–17.
- Suchý, V., Zachariáš, J., Tsai, H.C., Yu, T.L., Shen, C.C., Svetlik, I., Havelcová, M., Borecká, L., Machovíč, V., 2019. Relict Pleistocene calcareous tufa of the Chlupáčova sluj Cave, the Bohemian Karst, Czech Republic: a petrographic and geochemical record of hydrologically-driven cave evolution. *Sediment. Geol.* 385, 110–125.
- Sumita, M., Schmincke, H.U., 2013. Impact of volcanism on the evolution of Lake Van I: evolution of explosive volcanism of Nemrut Volcano (eastern Anatolia) during the past > 400,000 years. *Bull. Volcanol.* 75, 1–32.
- Teboul, P.A., Durlet, C., Gaucher, E.C., et al., 2016. Origins of elements building travertine and tufa: New perspectives provided by isotopic and geochemical tracers. *Sediment. Geol.* 334, 97–114.
- Verrecchia, E.P., Trombino, L., 2021. *A Visual Atlas for Soil Micromorphologists*. Springer Nature.
- Viles, H.A., Tailor, M.P., Nicoll, K., Neumann, S., 2007. Facies evidence of hydroclimatic regime shifts in tufa depositional sequences from the arid Naukluft Mountains, Namibia. *Sediment. Geol.* 195 (1–2), 39–53.
- York, D., Evensen, N.M., Martinez, M.L., De Basabe Delgado, J., 2004. Unified equations for the slope, intercept, and standard errors of the best straight line. *Am. J. Phys.* 72, 367–375. <https://doi.org/10.1119/1.1632486>.